Journal of ELECTRONIC MATERIALS
https://doi.org/10.1007/s11664-020-08422-1

A Comparasion of Photocatalytic Activity Between FeS_2, Ni-Doped FeS_2 Nanoparticles and Un-Doped FeS_2/rGO Composite

HONG QUANG NGUYEN,[1] THI HONG TUYET PHAN,[1] DINH QUANG HO,[1] HOA DU NGUYEN,[1] THE TAM LE,[1] THI MINH NGUYEN,[1] VAN THINH PHAM,[2] NGOC HUYEN DUONG,[3] and THI QUYNH HOA NGUYEN [1,4]

1.—Vinh University, 182 Le Duan, Vinh, Vietnam. 2.—NTT Hi-Tech Institute, Nguyen Tat Thanh University, Ho Chi Minh, Vietnam. 3.—Hanoi University of Technology, 1 Dai Co Viet, Hanoi, Vietnam. 4.—e-mail: ntqhoa@vinhuni.edu.vn

Un-doped and Ni-doped FeS_2 nanoparticles (NPs) with a doping concentration of 4.0 at.% have been synthesized by a solvothermal method. The obtained materials have been characterized by means of XRD, SEM, BET, Raman and UV–VIS spectroscopy. The photocatalytic activity has been evaluated based on degrading methylene blue with thin films of the NPs under UV–VIS light irradiation. An important observation was that the activity increases in the sequence FeS_2 NPs $\rightarrow$ Ni-doped FeS_2 NPs $\rightarrow$ composite of FeS_2 NPs/rGO. The enhanced energy gap and enlarged surface area, achieved by the Ni-doping and adding rGO were considered to be the main reason for the improved photocatalytic activity. Additionally, the mechanism of degradation has been studied using several scavengers. The photo-generated $\cdot OH$ and $\cdot O_2^-$ have shown to be dominant radicals in the visible light MB degradation. The presented data strongly suggest that the composite of FeS_2 NPs/rGO may be an efficient heterogeneous photo-catalyst for the degradation of the organic contaminant and water treatment. The proposed film forms of materials are promising for convenient reuse after a low-cost cleaning.

Key words: FeS_2, Ni-doped FeS_2, rGO, photocatalytic activity

INTRODUCTION

Metal sulphides have attracted considerable interest due to their promising properties for electronic, optical and optoelectronic applications.[1,2] Among them, FeS_2 is an abundant, non-toxic and low-cost material with small band gaps (0.95 eV) [3] and high absorption coefficients, which make it suitable for photovoltaics, lithium-ion batteries and hydrogen evolution.[4–7] FeS_2 was also employed for the photocatalytic degradation of several organic pollutants.[8–10] Up to now, FeS_2 NPs have been prepared by several methods, such as hot injection,[7,8,11,12] hydrothermal[6,10,13–15] and solvothermal methods.[16,17] Large-scale production of FeS_2 NPs can be obtained via both hydrothermal and solvothermal methods. However, compared with solvothermal method, the hydrothermal approach has the disadvantage for improvement of the permissibility and specific area of FeS_2 particles owing to the tendency to aggregate and form large particles during the synthesis process.[18] Therefore, the large-scale synthesis of high-dispersive FeS_2 NPs is still a challenge for strengthening their unique properties. Recently, doping with metal ions such as Fe and Co ions is an efficient way to enhance the photocatalytic performance of the photocatalysts.[19–21] For example, microwave hydrothermal synthesis of Co-doped FeS_2 showed a higher visible light photocatalytic performance

(Received April 6, 2020; accepted August 14, 2020)

Published online: 27 August 2020

than that of the pristine FeS_2.[19] However, little information is available on the solvothermal synthesis of FeS_2 NPs with controllable in situ doping of Ni and their photocatalytic activities.

Graphene, an attractive two-dimensional carbon 35 material, possesses excellent charge carrier and electron mobility, leading to effective separation of photogenerated carriers.[22,23] In fact, the introduction of rGO to Fe_3O_4 NPs has been observed to improve charge transfer between rGO sheets and organic dyes, enhancing photocatalytic activity of Fe_3O_4 NPs. Moreover, GO used as an attractive material in this field owing to its unique two-dimensional lamellar structure, large surface area, and full surface accessibility.[18,24] In addition, graphene or GO is not only able to prevent the aggregation of immobilized particles but also improves the overall catalytic activity owing to the synergistic effects between both components.[18,24] Experimentally, using a combination of FeS_2 and rGO has effectively improved the photocatalytic activities in removing 4-chlorophenol.[18] In the case of GO- Fe_3O_4 hybrid material, the observed enhancement in catalytic activity was attributed to the synergistic effects between of the adsorptive power of GO sheets and the hydroxyl radicals produced by heterogeneous photo-Fenton reactions.[24]

In this study, un-doped and Ni-doped FeS_2 NPs were synthesized by a low-cost, environment-friendly solvothermal method. The influence of Ni dopant and combination of FeS_2 NPs and rGO on photocatalytic activity of these composite systems were investigated and evaluated.

EXPERIMENTAL DETAILS

Materials

Graphite flakes were purchased from Sigma. Sulphuric acid (H_2SO_4), sodium nitrate ($NaNO_3$), potassium permanganate ($KMnO_4$), hydrochloric acid (HCl), hydrogen peroxide (H_2O_2), iron (II) acetylacetonate ($C_{10}H_{14}FeO_4$), nickel (II) chloride hexahydrate ($NiCl_2.6H_2O$), oleyamnine (70%), 1,2 hexadecandiol, sulphur flakes, hydrazine monohydrate (98 wt.%), ethanol (99.5%), methanol (anhydrous, 99.8%), toluene (99.9%) and cyclohexane (99.5%) were obtained from Sigma-Aldrich. The 2×2 cm^2 microscopic glass substrates were used after cleaning by sonication in acetone, methanol and deionized (DI) water.

Synthesis and Characterization of un-Doped and Ni-Doped FeS_2 NPs

The un-doped and Ni-doped FeS_2 NPs were synthesized via a solvothermal method. In a typical synthesis, 7.5 mL of oleylamine was added into a 50-mL Teflon-lined stainless steel autoclave containing 0.25 mmol of iron (II) acetylacetonate, 0.25 mmol of 1,2 hexadecandiol, 1.5 mmol of sulfur flakes. For the synthesis of Ni-doped FeS_2 NPs, we added 0.025 mmol of nickel (II) chloride hexahydrate. The reaction mixture was sonicated for 1 h to ensure homogenous mixing. The reaction temperature was fixed at 190°C, and the reaction time was 20 h. The autoclave was then cooled to room temperature naturally and the precipitate was collected via centrifugation. After the reaction period, the pure FeS_2 NPs and Ni-doped FeS_2 NPs samples were washed with methanol and toluene, then dried in air before collection for further characterization.

The phase quality of the FeS_2 and Ni-doped FeS_2 NPs was analysed by X-ray diffraction (XRD) using a D8 Advance Brüker diffractometer using CuKα (λ = 1.5406 Å) radiation and Raman spectra using a LabRAM HR800 (Horiba) with a 632.8 nm excitation laser at a resolution of 1.0 cm^{-1}. The surface morphology was studied in a scanning electron microscope (SEM, JEOL JCM-6000Plus). Specific surface area of FeS_2 NPs, Ni-doped FeS_2 NPs and composite of FeS_2 NPs and rGO was determined by the Brunauer–Emmett–Teller (BET) method using a Micromeritics Gemini VII 2390t analyzer at 77 K. The optical absorption spectra were obtained using ultraviolet–visible spectroscopy (Agilent, 8453). The Ni doping concentration was determined to be 4 at.% as analysed by an inductively coupled plasma mass spectrometry (ICP-MS, 79 Perkin Elmer ELAN 9000).

Synthesis and Characterization of Graphene Oxide

Graphene oxide was synthesized from graphite flakes using the modified Hummers method.[25] The detailed synthesis and characterization were carried out as described in our previous study.[26] The GO dispersion was suspended in DI water with concentration of 2 mg/mL.

Preparation of Films of un-Doped, Ni-Doped FeS_2 NPs and Composite Made Up of FeS_2 NPs and Reduced Graphene Oxide

The recovery and reuse of photocatalyst is a key factor for large-scale application. To facilitate the process of photocatalyst recovery and to reduce the agglomeration problems of suspended NPs, we propose to evaluate photocatalytic activity from the films of un-doped, Ni-doped FeS_2 NPs, and composite made up of FeS_2 NPs and rGO. The films were deposited by spray pyrolysis onto a 2×2 cm^2 glass substrate using an airbrush system with a nozzle diameter of 0.2 mm. The inlet pressure was fixed at 3 bar. The distance between the tip of the nozzle and the substrate was kept at 8 cm. The volume of the spray solution is 2 mL. The solution of GO, rGO, FeS_2 NPs, and composite of FeS_2 NPs and rGO were used to fabricate the films shown in Fig. 1(a)–(d). The final films of undoped, Ni-doped FeS_2 NPs and composite of FeS_2 NPs and rGO (here and after denoted as [FeS_2 NPs/rGO]) were obtained

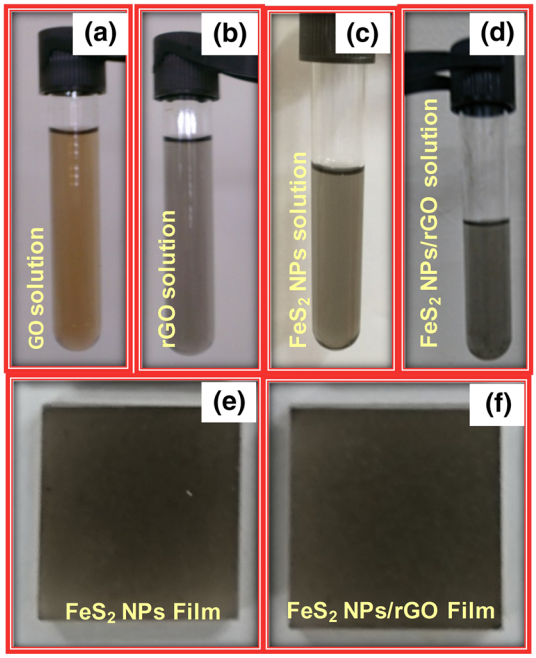

Fig. 1. Optical photographs of (a) GO, (b) rGO, (c) FeS_2, and (d) FeS_2 NPs and rGO solutions. Digital image of fabricated (e) FeS_2 NPs film and (f) FeS_2 NPs/rGO film.

after the spray deposition. Since the film of Ni-doped NPs was obtained to be similar to that of un-doped, we show only the features of the un-doped FeS_2 and [FeS_2 NPs/rGO], respectively, in Fig. 1(e) and (f).

For the growth of un-doped and Ni-doped FeS_2 NPs films: The initial FeS_2 NPs or Ni-doped FeS_2 NPs solutions (20 mg/mL) were created by diluting respective constituents in cyclohexane. The growth temperature was fixed at 100°C.

For the growth of the composite of FeS_2 NPs and rGO film: The GO dispersion (2 mg/mL) was vigorously mixed with hydrazine monohydrate with a volume ratio of 1:2 for 5 min and then diluted 10 times with DI water/ethanol/hydrazine monohydrate with a volume ratio of 1:1:2. Sonication was then applied using a sonication bath for 1 min in order to obtain stable and homogeneous GO-hydrazine dispersion (referred to as rGO solution). Finally, the FeS_2 NPs (20 mg/mL) and GO-hydrazine (0.2 mg/mL) solution with the volume ratio of 1:1 were sonificated for 5 min to ensure a homogeneous mixing. The growth temperature was fixed at 200°C in order to obtain proper rGO in the composite.[27]

Photocatalytic Activity

The photocatalytic activity was studied by measuring the decomposition of methylene blue (MB) in aqueous solution using UV–VIS spectroscopy. In each experiment, the suitable film of FeS_2 NPs, Ni-doped FeS_2 NPs or composite of FeS_2 NPs/rGO was submerged into 10 mL of MB aqueous solution with a concentration of 10^{-5} M, denoted as MB solution. The prepared set was stored in the dark for 30 min to reach adsorption equilibrium before illumination. The white light of a tungsten light bulb (100 W) and UV light of 365 nm (6 W) were used as visible-light and UV irradiation sources, respectively.[28] At the fixed time intervals of illumination, a quantity of 0.75 mL from the MB solution was taken out and measured by UV–VIS spectrometry at a maximum absorption of MB (665 nm).

To find the mechanism responsible for MB degradation, several scavengers such as ethylenediaminetetraacetic acid (EDTA-2Na), p-benzoquinone (BQ) and isopropyl alcohol (IPA) have been utilized as holes, superoxide radical $\cdot O_2^-$ and hydroxyl radical $\cdot$OH trapping agents. In the scavenging test, 0.2 mmol of these active species scavengers were added individually during the photocatalytic reaction. The method of active species trapping experiment is similar to the photocatalytic activity experiment.

RESULTS AND DISCUSSION

Figure 2 shows SEM image of the un-doped and Ni-doped FeS_2 NPs samples. All the samples exhibit uniform morphology and particle size distribution. The smaller NPs are obtained in the NP sample with Ni doping. The size of undoped and Ni-doped FeS_2 NPs is estimated approximately to be 200–300 nm and 80–150 nm, respectively. A similar observation was reported for those of FeS_2 NPs with Co incorporation.[29]

Figure 3 shows XRD patterns of the un-doped and Ni-doped FeS_2 NPs samples. It is seen that both un-doped and Ni-doped FeS_2 NPs samples show similar XRD patterns. The discernible peaks can be indexed as those for pyrite FeS2 (JCPDS No. 01-079-0617). Fitting of X-ray data for our samples using Rietveld profile refinement yields lattice parameters a = 0.54173(2) nm with goodness of fit χ^2 of 2.78 for un-doped and a = 0.5316(3) nm with χ^2 = 3.32 for Ni-doped NPs. We must admit that there are several un-indexed peaks in the low range, which is probably associated with a foreign phase in these samples. However, the quantity of the impurities is low, comparable to the detection limit of X-ray spectrometry. The crystallite size can be calculated from the Scherrer equation:

$$L = \frac{K\lambda}{\beta\cos\theta}, \tag{1}$$

where λ is the X-ray wavelength, β is the peak width at half maximum height of the diffraction reflection, and K is a constant related to crystallite shape, normally taken as 0.9 for spherical crystals with cubic unit cell. Using Eq. (1), we estimated the crystallite size of the studied samples, taking into account the average of six most intense peaks of each phase. It turns out that the un-doped FeS_2 NP sample shows a crystallite size of $\sim$ 20 nm, while the Ni-doped FeS_2 NP sample exhibit a little smaller

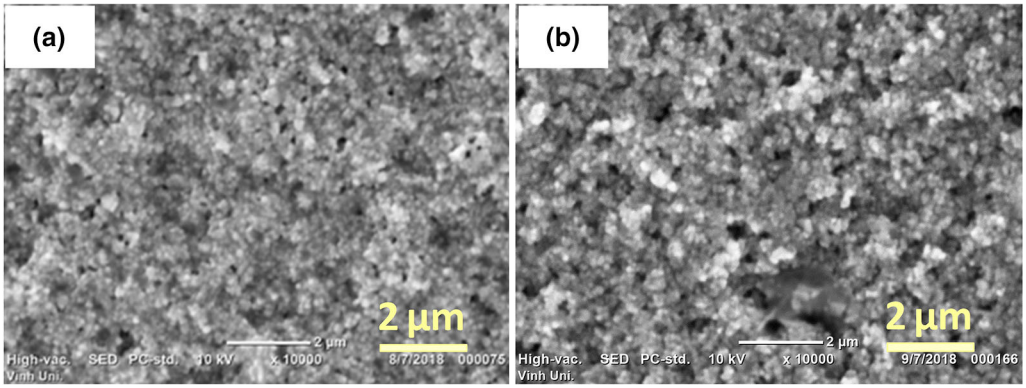

Fig. 2. SEM images of (a) the un-doped and (b) Ni-doped FeS_2 NPs.

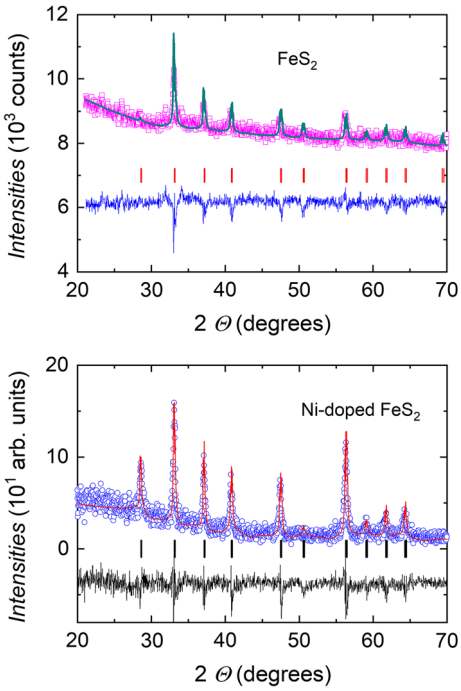

Fig. 3. XRD patterns of the un-doped (upper panel) and Ni-doped (lower panel) FeS_2 NPs. The points are experimental data while the solid lines present theoretical profiles. The vertical bars indicate the indexed positions of the Bragg reflection and the bottom line is the difference between the experimental and theoretical data.

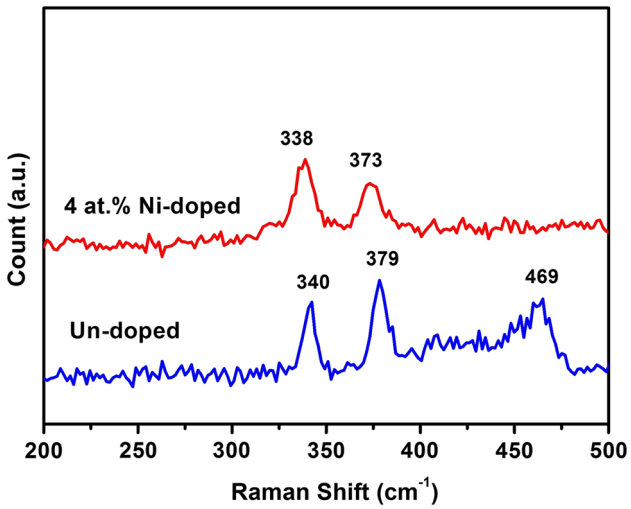

Fig. 4. Raman spectra of un-doped and Ni-doped FeS_2 NPs.

size of ~ 17 nm. It may be said that even for the un-doped FeS_2 NP sample, the calculated average grain sizes appear smaller than the observed NPs shown in Fig. 2, so it is likely that each NP consists of multiple grains or the agglomerate of NPs. In a semiconductor photocatalyst, a smaller crystallite size typically allows a better charge transport in the structure, reducing the recombination and increasing the efficiency of the photocatalytic reaction.

The measurements of N_2 adsorption–desorption isotherms provided specific surface areas of the studied samples. The BET values of FeS_2 NPs, Ni-doped FeS_2 NPs and a composite of FeS_2 NPs/rGO were found to be 16.5, 26.0 and 99.1 m^2/g, respectively, indicating that the Ni-doping or introduction of rGO significantly increases the surface areas of the FeS_2-based sample.

Raman spectroscopy, based on an inelastic light-scattering, detects the molecule-specific vibrations in a sample irradiated by a monochromatic laser.[30] Thus, this technique basically provides information about the phonon vibrational modes and obviously is very sensitive to phases and composition of an investigated sample. In consequence, Raman spectroscopy may be applied to examine the phase purity of NPs, for instance, as reported in Ref. 31 The Raman spectra of the un-doped and Ni-doped FeS_2 NP samples are shown in Fig. 4. For both studied compounds, we observed two strong peaks near 340 and 379 cm^{-1}, which correspond well with the reported values for disulphide phonons E_g and A_g modes of FeS_2 pyrite.[12,13,16,30,31] The peak near 340 cm^{-1} describes vibrational and stretching modes [30,32] and the secondary high peak near 379 cm^{-1} usually assigned to the in-phase stretching vibration of the S–S pair.[16,29,30] This finding indicates that the Ni^{2+} ion was substituted correctly into the FeS_2 matrix. The same phenomenon was observed in Co-doped FeS_2 particles.[18] It is noted

that the spectrum of the un-doped sample exhibits additionally a strong peak at 469 cm^{-1}, which was assigned due to elemental sulphur.[30] Nonetheless, the Raman spectrum of single-crystalline FeS_2 displays a mode 430 cm^{-1} associated with symmetry T_g. This mode is detected in measurement configuration of vertical polarizations of the incident and scattered radiation. We may emphasize that un-doped and Ni-doped FeS_2 NPs have no other peaks originating from impurities, suggesting the high phase purity of our samples. It is interesting that the Raman peaks of the Ni-doped FeS_2 NP sample shifts to a lower wavenumber compared to those of un-doped. Usually, shifting Raman peaks is related to the changes in chemical bond length of molecules. In our case, the phenomenon occurs due to longer bonds in the Ni-doped FeS_2 NPs. Moreover, the Raman shifts ω have been considered by Liu et al. [33] to be dependent on nanoparticle sizes D. The authors developed a relation $\omega(D)$ for nanomaterials: $\omega(D) \propto (B_a/B_t)^{1/4}$, where B_a and B_t are geometric parameters related to the size and shape of the system. Experimental data have demonstrated in several nanosized semiconductors that as size decreases, $\omega(D)$ gradually drops. Accordingly, the Raman spectroscopy data for un-doped and Ni-doped FeS_2 NPs can confirm smaller nanosizes in the Ni-doped FeS_2 NP samples. By the way, a larger bandwidth in the Ni-doped FeS_2 NP sample may also be indicative of larger structural disorders.

Figure 5 presents the absorption spectra of the un-doped and Ni-doped FeS_2 NPs measured in the wavelength range 180–1100 nm. For comparison, we show in the inset of Fig. 5 the data for the GO and rGO solutions. Characteristic peaks in the absorption spectra of GO and rGO (designed by arrows) are observed at 230 and 295, and 265 nm, respectively. The peaks of 230 nm and 265 nm result from $\pi - \pi^*$ transition of aromatic $C = C$ bonds, whereas the shoulder peak of 295 nm is due to $n - \pi^*$ transition of aromatic $C = O$ bonds.

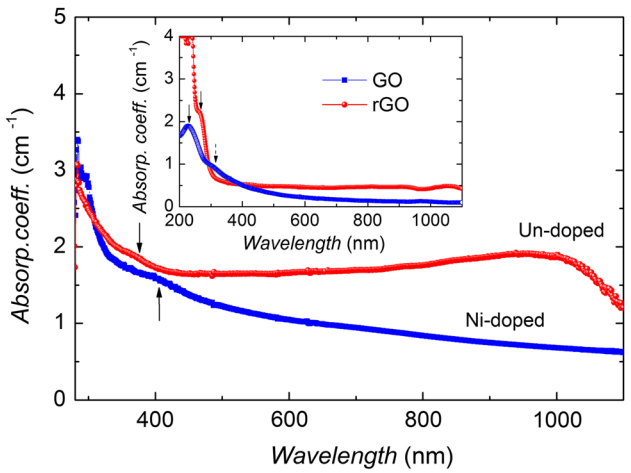

Fig. 5. UV-VIS spectra of the un-doped and Ni-doped FeS_2 NP samples, and of GO and rGO in the inset.

Our results fully agree with the data reported in literature, e.g.[34] In the case of the un-doped and Ni-doped FeS_2 NPs, UV–VIS spectroscopy reveals a shift in absorption peaks too (see the positions of absorption peaks denoted by arrows). The absorption edge of the un-doped FeS_2 NPs can be evaluated to be $\sim$ 600 nm, which moves to $\sim$ 700 nm in the Ni-doped FeS_2 NP sample. Thus, the Ni-doping shifts the absorption edge into the visible-light region.

The energy of the optical bandgap (E_g) is estimated using Tauc plots by plotting $(\alpha h\nu)^n$ versus $h\nu$ with $n = 1/2$ for indirect transition and $n = 2$ for direct transitions.[29,31,35,36] Actually, Fig. 6 (a)–(d) presents the energy of bandgaps for GO, rGO, un-doped and Ni-doped FeS_2 NPs, respectively. The obtained values of energy gaps are given in Table I. Our measurement indicates a decrease in direct gap but an increase in indirect gap values of GO due to reduction to rGO. For un-doped and Ni-doped FeS_2 NPs, we observe the indirect bandgaps of 1.12 and 1.2 eV, respectively, whereas, the first and second direct transitions were found to amount to 2.41 and 3.47 eV, and 2.25 and 3.56 eV, respectively. The indirect bandgap of both un-doped and Ni-doped NPs was wider than that of bulk pyrite of about 0.95 eV.[3] The similar observation was obtained in previous works.[29,31,35,36] The first and second direct transitions have been previously studied experimentally by analysing band-edge absorption of cubic pyrite NPs [31,35,36] and theoretically from density functional theory (DFT) calculations.[37,38] Apparently, the estimated values of the first direct transition of both un-doped and Ni-doped FeS_2NPs are close to those determined experimental measurement (2.24 eV) [8] and (2.4 eV) [29] and theoretical calculation (2.1 eV).[38] The values of the second direct transition of both un-doped and Ni-doped FeS2 NPs are close to the theoretical value (3.5 eV) [38] but higher than the experimental value (2.9–3.0 eV).[31,35]

Photocatalytic activity of the un-doped FeS_2 NPs, Ni-doped FeS_2 NPs, and [FeS_2 NPs/rGO] samples were evaluated by measuring the decomposition of methylene blue in an aqueous solution. Figure 7 shows the changes in MB concentration as a function of irradiation time under both UV and visible light. As seen in Fig. 7(a), the un-doped NPs decompose methylene blue effectively through photocatalytic reaction under visible light irradiation due to its narrow bandgap energy. Compared with the un-doped NPs, the Ni-doped FeS_2 NPs sample shows much higher photocatalytic activity (Fig. 7a). The Ni doping can decrease the NP size, resulting in an increase of its specific surface area and improving the visible-light photocatalysis. This interpretation has previously been proposed for an enhanced photocatalytic performance of Co-doped FeS_2 nanoparticles.[19] Moreover, in Ni-doping the conductivity of the carriers is higher by one order of magnitude over undoped FeS_2,[39] leading to a fast

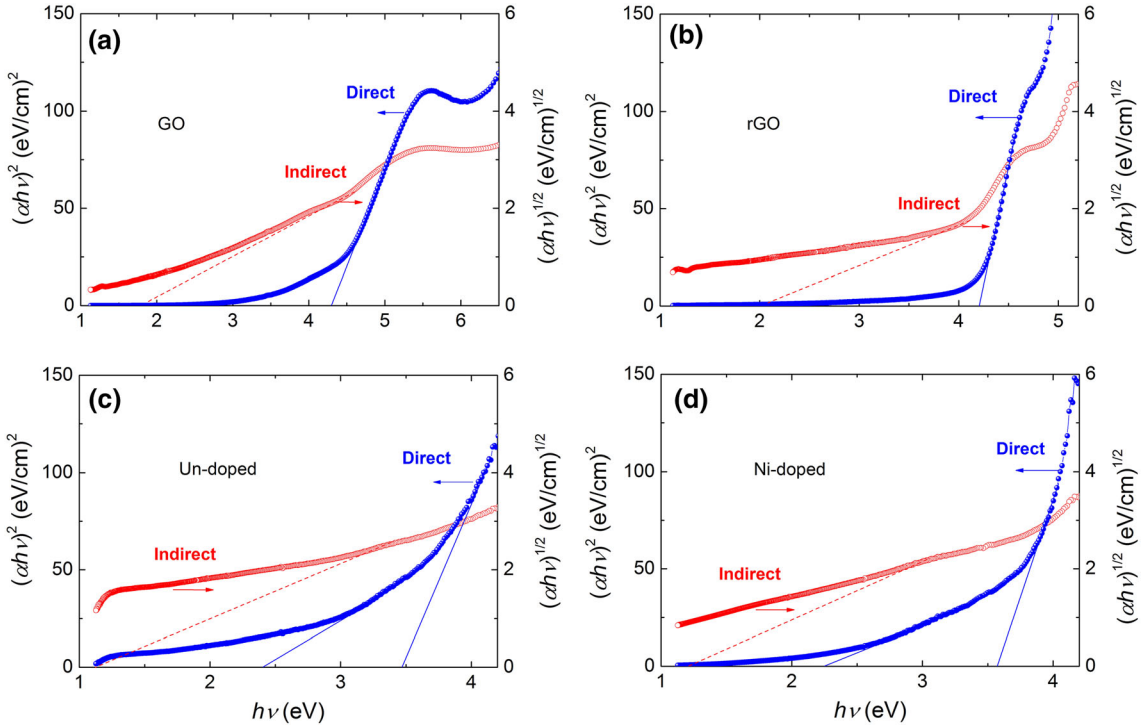

Fig. 6. Plotting $(\alpha h\nu)^n$ versus $h\nu$ with n = 1/2 for indirect transition (red dash line) and n = 2 for direct transitions (blue solid line) of (a) GO, (b) rGO, (c) undoped FeS_2 NPs, and (d) Ni-doped FeS_2 NPs.

Table I. The direct and indirect gaps of GO, rGO, un-doped and Ni-doped FeS_2 NPs

Samples	Direct band (eV)	Indirect band (eV)
GO	4.29	1.83
rGO	4.20	2.07
Un-doped	2.41, 3.47	1.12
Ni-doped	2.25, 3.56	1.20

charge transport. Another mechanism is associated with the shifting absorption edge into the visible-light regime in the Ni-doped FeS_2 NPs sample (see Fig. 7d), so the visible-light photocatalytic performance becomes enhanced.

Furthermore, the composite of FeS_2 NPs and GO studied in the work clearly improves the visible-light photocatalytic properties compared to pure FeS_2 NPs or Ni-doped FeS_2 NPs. This can be attributed to the unique properties of GO and rGO such as larger surface area, full surface accessibility and fast charge transport and the synergistic effects between both components of GO or rGO and NPs.[18,23,24,40]

Under UV irradiation, the FeS_2 NP and rGO composite samples also show much stronger photocatalytic activity than the un-doped and Ni-doped FeS_2 NP samples (Fig. 7b). Compariing with the VIS data, one recognizes that there is greater photoactivity in the visible-light region. The principle reason is probably due to different powers of used irradiation sources. Moreover, the MB photodegradation clearly obeyed the first-order reaction kinetics: $C = C_o exp(-kt)$, where C_o is the initial concentration of reactant C at time $t = 0$ and k is the reaction rate. The linearized kinetic plots, $\ln(Co/C)vst$, for the degradation of MB with the presence of the un-doped FeS-$_2$ NPs, Ni-doped FeS_2 NPs, and [FeS_2 NPs/rGO] samples under UV and visible-light irradiation are shown in Fig. 7(c) and (d).

The degradation of MB corresponds approximately to the first-order kinetics and the observed rate constants of UV and visible-light photocatalytic degradation are gathered in Table II. Our results of the Ni-doped FeS_2 NPs sample exhibit comparative activity with the data published by Wang et at. for Co- and Ni-doped FeS_2.[41] However, it must be pointed out that the [FeS_2 NPs/rGO] sample reveals the highest k values, which are almost of two times larger than those un-doped or Ni-doped FeS_2 NPs samples. This means that highest degradation efficiency of MB can be achieved by a combination of FeS_2 NPs/rGO, whereas the Ni-doping has minimal effect on the photocatalic activity.

One of the tasks of this work was to explore the mechanism of the photoactivity under visible-light irradiation. In general, we must seek photoinduced free radicals or photogenerated charges and their recombination from the pair $(h^+ + e^-)$. In most cases, the electron paramagnetic resonance (EPR) spectroscopy was successfully employed, since the technique allows us to investigate the change in

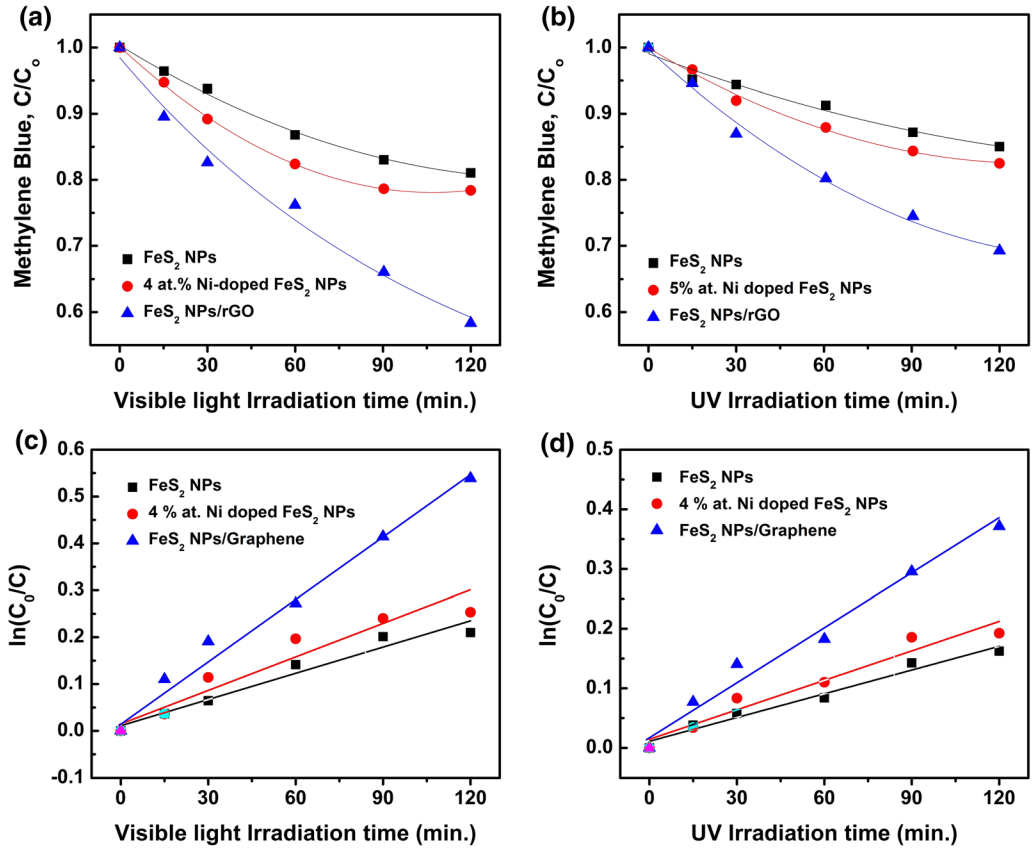

Fig. 7. Photocatalytic properties of the un-doped NPs sample (solid squares), Ni-doped FeS_2 NPs sample (solid circles) and the FeS_2 NPs and rGO composite under (a) visible light and (b) UV irradiation. The linearized kinetic plots for the degradation of MB with the presence of the corresponding photocatalyst samples under (c) visible light and (d) UV irradiation.

Table II. The reaction rates under UV and VIS irradiation k_{UV} and k_{VIS} (10^{-3} min^{-1})

Samples	k_{UV}	k_{VIS}
FeS_2 NPs	1.87	1.33
Ni-doped Fe_2 NPs	2.17	1.65
FeS_2 NPs/rGO	4.3	2.95

structure and electronic properties due to light irradiation.[42–44] Unfortunately, EPR is not advisable for Ni-doped FeS_2 because the EPR spectra of spin S = 1 are forbidden, which causes interpretation difficulties.[45,46] An alternative, effective method for determination of free radicals in the photocatalytic process is based on using radical scavengers as trapping agents. Free radicals generated during photocatalytic reaction include superoxide $\cdot O_2^-$ and hydroxyl radical $^{\cdot}OH$, which can be trapped by BQ and IPA scavenger, respectively. So, we have undertaken a study on the photocatalytic activity of the FeS_2-based catalysts with respect to applied scavengers. The effect of EDTA-2Na, BQ and IPA on the photoactivity of FeS_2 NPs, Ni-doped FeS_2 NPs and a composite of FeS_2 NP/rGO under VIS irradiation is presented in Fig. 8 (a), (b) and (c), respectively. It can be found that by using IPA as the trapping agent the photocatalytic degradation in all the three studied catalysts decreases drastically, indicating that $^{\cdot}OH$ radicals are the main active groups in the degradation reaction of MB. Otherwise, if using BQ as the scavenging agent, the photocatalytic activity decreases a lesser extent, meaning a certain responsibility of super oxide $\cdot O_2^-$ radicals merely in the photocatalytic MB degradation. From the experiment, one sees also that the photocatalytic degradation of MB using EDTA-2Na as the scavenger is similar to that without scavenger. Therefore, the photogenerated hole transfer is not a suitable mechanism for MB degradation by the FeS_2-based materials. Instead, a possible process of MB photodegradation follows the reactions:

(i) FeS_2-based catalyst + $h\nu \rightarrow$ FeS_2-based catalyst + $(h^+ + e^-)$
(ii) $e^- + O_2 \rightarrow \cdot O_2^- + H_2O$
(iii) $\cdot O_2^- + H_2O \rightarrow \cdot OH$
(iv) $h^+ + H_2O \rightarrow \cdot OH$

yielding the photogenerated $^{\cdot}OH$ and $\cdot O_2^-$ charges from trapping sites.

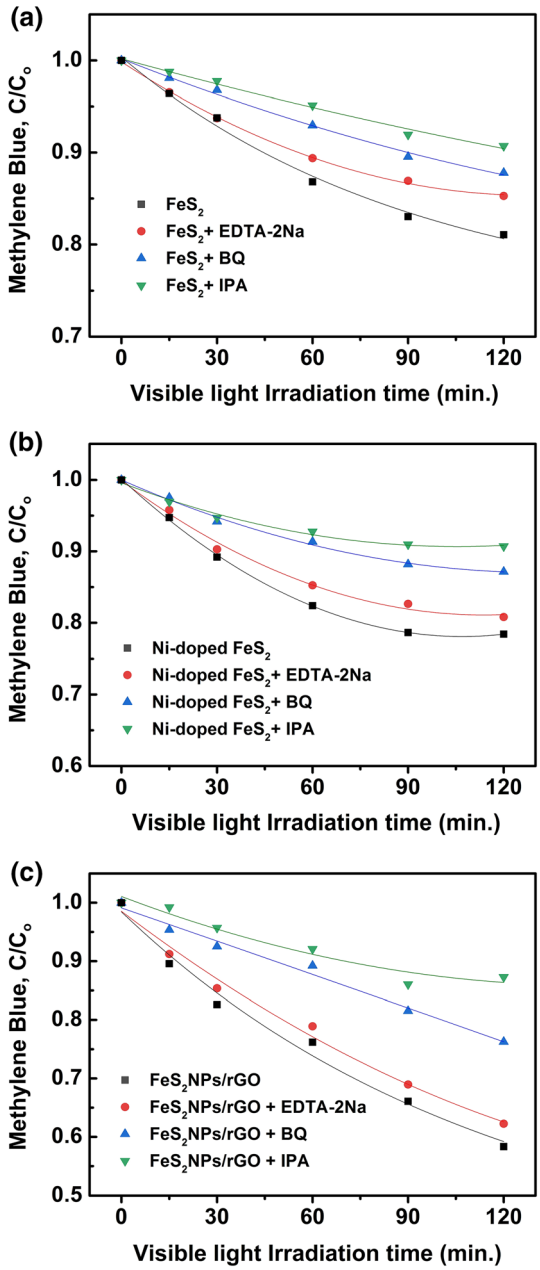

Fig. 8. The photocatalytic activity of (a) the undoped FeS_2 NPs, (b) the Ni-doped FeS_2 NPs, and (c) the composite of FeS_2 NPs/rGO catalyst in the presence of EDTA-2NA, BQ, and IPA scavengers.

CONCLUSIONS

A solvothermal technique was utilized to synthesize the un-doped and Ni-doped FeS_2 NPs with a doping concentration of 4.0 at.%. The un-doped and Ni-doped FeS_2 NPs have a single-crystalline structure of the pyrite phase. The photocatalytic activity of the films of the un-doped and Ni-doped FeS_2 NPs and composite of FeS_2 NPs/rGO fabricated by spray pyrolysis have been investigated. Larger energy gap, smaller size and larger specific area of the NPs were achieved by Ni-doping, which seem to be the main reason for the improved photocatalytic activity of Ni-doped FeS_2 NPs. Furthermore, the composite of FeS_2 NPs and rGO exhibit higher UV and visible-light photocatalytic compared with both un-doped and Ni-doped FeS_2 NPs, separately. The photocatalytic degradation mechanism was investigated by means of using EDTA-2Na, BQ and IPA scavenger. The possible photocatalytic process can be described based on the free $^{\cdot}OH$ and $\cdot O_2^-$ radical generation. Thanks to considerably enhanced photoactivity of the composite of FeS_2 NPs and rGO, this heterogeneous material is a promising candidate for the degradation of organic contaminants and water treatment. We believe that the film forms of photoactive catalysts are suitable for multiple utilisation and for convenient reuse after a low-cost cleaning.

CONFLICT OF INTEREST

The authors declare that they have no conflict of interest.

REFERENCES

1. C.-H. Lai, M.-Y. Lu, and L.-J. Chen, *J. Mater. Chem.* 22, 19 (2012).
2. A.M. HuertaFlores, L.M. Torres Martinez, E. Moctezuma, A.P. Singh, and B. Wickman, *J. Mater. Sci.: Mater. Electron.* 29, 11613 (2019).
3. A. Schlegel and P. Wachter, *J. Phys. C: Solid State Phys.* 9, 3363 (1976).
4. M.C. Acevedo, N.S. Kaiser, C.R. English, D. Liang, B.J. Thompson, H.E. Chen, K.J. Czech, J.C. Wright, R.J. Hamers, and S. Jin, *J. Am. Chem. Soc.* 136, 17163 (2014).
5. C. Song, S. Wang, W. Dong, X. Fang, J. Shao, J. Zhu, and X. Pan, *Sol. Energy* 133, 429 (2016).
6. W.L. Liu, X.H. Rui, H.T. Tan, C. Xu, Q.Y. Yan, and H.H. Hng, *RSC Adv.* 4, 48770 (2014).
7. D. Jasion, J.M. Barforoush, Q. Qiao, Y. Zhu, S. Ren, and K.C. Leonard, *ACS Catal.* 5, 116653 (2015).
8. L. Zhu, B.J. Richardson, and Q. Yu, *Nanoscale* 6, 1029 (2014).
9. G. Kaur, B. Singh, P. Singh, M. Kaur, K.K. Buttar, K. Singh, A. Thakur, R. Bala, M. Kumar, and A. Kumar, *RSC Adv.* 6, 99120 (2016).
10. V.G. Morales, A.M. Ayala, M. Pal, M.A. Cortes, J.A. Toledo, and N.R. Mathews, *Chem. Phys. Lett.* 660, 93 (2016).
11. J. Puthussery, S. Seefeld, N. Berry, M. Gibbs, and M. Law, *J. Am. Chem. Soc.* 133, 716 (2010).
12. M. Alam Khan, M.O. Manasreh, and Y.M. Kang, *Mater. Lett.* 126, 181 (2014).
13. Y. Liang, P. Bai, J. Zhou, T. Wang, B. Luo, and S. Zheng, *Cryst. Eng. Comm.* 18, 6262 (2016).
14. C. Wadia, Y. Wu, S. Gul, S.K. Volkman, J. Guo, and A.P. Alivisatos, *Chem. Mater.* 21, 2568 (2009).
15. B. Yuan, W. Luan, and S.T. Tu, *Dalton Trans.* 279, 772 (2012).
16. B. Yuan, W. Luan, S.T. Tu, and J. Wu, *New J. Chem.* 39, 3571 (2015).
17. S. Kar and S. Chaudhuri, *Chem. Phys. Lett.* 398, 22 (2004).
18. W. Liu, L. Xu, X. Li, C. Shen, S. Rashid, Y. Wen, W. Liu, and X. Wu, *RSC Adv.* 5, 2449 (2015).
19. F. Long, J. He, M. Zhang, X. Wu, S. Mo, Z. Zou, and Y. Zhou, *J. of Mater. Sci.* 50, 1848 (2015).
20. N.T.Q. Hoa, Z. Lee, and E.T. Kim, *J. Electrochem. Soc.* 159, K42 (2012).
21. N.T.Q. Hoa, *Int. J. Nanotechnol.* 12, 426 (2015).
22. L. Zhang, Z. Bao, X. Yu, P. Dai, J. Zhu, M. Wu, G. Li, X. Liu, Z. Sun, and C. Chen, *ACS Appl. Mater. Interfaces.* 8, 6431 (2016).

23. Q. Xiang, J. Yu, and M. Jaroniec, *Chem. Soc. Rev.* 41, 782 (2012).
24. S. Guo, G. Zhang, Y. Guo, and J.C. Yu, *Carbon* 60, 437 (2013).
25. W.S. Hummers and R.E. Offeman, *J. Am. Chem. Soc.* 80, 1339 (1958).
26. V.D. Dao, N.T.Q. Hoa, L.L. Larina, J.-K. Lee, and H.S. Choi, *Nanoscale* 5, 12237 (2013).
27. V.H. Pham, T.V. Cuong, S.H. Hur, E.W. Shin, J.S. Kim, J.S. Chung, and E.J. Kim, *Carbon* 48, 1945 (2010).
28. L.T. Hung and N.T.Q. Hoa, *Electrochem. Solid-State Lett.* 15, K45 (2012).
29. T. Kinner, K.P. Bhandari, E. Bastola, B.M. Monahan, N.O. Haugen, P.J. Roland, T.P. Bigioni, and R.J. Ellingson, *J. Phys. Chem. C* 120, 5706 (2016).
30. J.R. Ferraro, K. Nakamoto, and C.W. Brown, *Introductory Raman Spectroscopy*, 2nd ed. (Amsterdam: Elsevier, 2003).
31. V. Toniazzo, C. Mustin, J.M. Portal, B. Humbert, R. Benoit, and R. Erre, *Appl. Surf. Sci.* 143, 229 (1999).
32. H. Xue, D.Y.W. Yu, J. Qing, X. Yang, J. Xu, Z. Li, M. Sun, W. Kang, Y. Tang, and C.-S. Lee, *J. Mater. Chem. A* 3, 7945 (2015).
33. H. Li, X.W. He, H.J. Xiao, H.N. Du, J. Wang, and H.X. Zhang, *Phys. Chem. Chem. Phys.* 19, 28056 (2017).
34. S. Yang, W. Yue, D. Huang, C. Chen, H. Lin, and X. Yang, *RSC Adv.* 2, 8827 (2012).
35. S. Khalid, M.A. Malik, D.J. Lewis, P. Kevin, E. Ahmed, Y. Khan, and P. O'Brien, *J. Mater. Chem. C* 3, 12068 (2015).
36. H.A. Macpherson, C.R. Stoldt, and A.C.S. Nano, *ACS Nano* 6, 8940 (2012).
37. V.N. Antonov, L.P. Germash, A.P. Shpak, and A.N. Yaresko, *Phys. Status Solidi B* 336, 411 (2009).
38. C. Steinhagen, T.B. Harvey, C.J. Stolle, J. Harris, and B.A. Korgel, *J. Phys. Chem. Lett.* 3, 2352 (2012).
39. S.W. Lehner, K.S. Savage, and J.C. Ayers, *J. Cryst. Growth* 286, 306 (2006).
40. Y. Chen, S. Xu, Y. Li, R.J. Jacob, Y. Kuang, B. Liu, Y. Wang, G. Pastel, L.G. Salamanca-Riba, M.R. Zachariah, and L. Hu, *Adv. Energy Mater.* 7, 1700482 (2017).
41. Y. Wang, X. Zhang, Y. Ji, and G. Zheng, *J. Wuhan Univ Technol.-Mat. Sci. Edit.* 33, 802 (2018).
42. D.C. Hurum, A.G. Agrios, K.A. Gray, T. Rajh, and M.C. Thurnauer, *J. Phys. Chem. B* 107, 4545 (2003).
43. S. Livraghi, M. Rolando, S. Maurelli, M. Chiesa, M.C. Paganini, and E. Giamello, *J. Phys. Chem. C* 118, 22141 (2014).
44. E.A. Konstantinova, A.I. Kokorin, A.A. Minnekhanov, T.V. Sviridova, and D.V. Sviridov, *Catal. Lett.* 149, 2256 (2019).
45. R.N. Chandler and R.W. Bené, *Phys. Rev. B* 8, 4979 (1973).
46. D. Siebert, R. Miller, S. Fiechter, P. Dulski, and A. Hartmann, *Z. Naturforschung A* 45, 1267 (1990).